

Influence of Atmospheric Turbulence Channel on a Ghost-imaging Transmission System

Kaimin Wang¹, Zhaorui Wang¹, Leihong Zhang^{1*}, Yi Kang¹, Hualong Ye¹,
Jiafeng Hu², and Jiaming Xu¹

¹Engineering Research Center of Optical Instrument and System, Ministry of Education and Shanghai Key Lab of Modern Optical System, University of Shanghai for Science and Technology, Shanghai 200093, China

²School of Physics and Electronics, East China Normal University, Shanghai 200093, China

(Received September 4, 2019 : revised November 22, 2019 : accepted December 7, 2019)

We research a system of compressed-sensing computational ghost imaging (CSCGI) based on the intensity fluctuation brought by turbulence. In this system, we used the gamma-gamma intensity-fluctuation model, which is commonly used in transmission systems, to simulate the CSCGI system. By setting proper values of the parameters such as transmission distance, refractive-index structure parameter, and sampling rates, the peak signal-to-noise ratio (PSNR) performance and bit-error rate (BER) performance are obtained to evaluate the imaging quality, which provides a theoretical model to further research the ghost-imaging algorithm.

Keywords : Ghost imaging, Atmospheric turbulence, Gamma-gamma model, Image transmission
OCIS codes : (010.1330) Atmospheric turbulence; (060.4510) Optical communications; (110.0115) Imaging through turbulent media; (110.1758) Computational imaging

I. INTRODUCTION

In recent years, quantum technology has flourished and quantum imaging technology has developed. *Ghost imaging* is one of the hot new imaging technologies. Ghost imaging utilizes properties of quantum entanglement to achieve nonlocal image transmission. Due to the existence of correlation characteristics, its anti-interference ability, weak optical imaging capability, and encryption capability have strong advantages, compared to traditional optics. However, since ghost imaging is still transmitted through the optical path, the image quality is inevitably affected by the quality of the optical path, and light is transmitted through the air, so atmospheric turbulence is inevitably an important factor affecting the associated imaging.

As a new imaging method, associative imaging has attracted wide attention in the field of image transmission [1-9]. Ghost-imaging techniques continue to evolve, from entangled photon pair [1] to thermal sources [2], from traditional ghost imaging to computational ghost imaging

(CGI) [3], and many improved methods such as compressed sensing (CS) [4] and differential correlation imaging [5] have also been proposed. With the improvement of image quality, the influence of turbulence on imaging has attracted more and more attention. In reference [6], a random phase screen was applied to simulate the phase disturbance of turbulence. In reference [7], a thermo-optical ghost-imaging experiment was carried out to verify that it is turbulence-free. In reference [10], the visibility and quality of the ghost image through monostatic turbulence and bistatic turbulence were discussed. In reference [11], numerical calculations to demonstrate atmospheric effects on ghost imaging of a double slit were studied. In reference [12], the spatial resolution, image contrast, and SNR were calculated for ghost imaging through turbulence on rough-surfaced targets. However, the above references rarely research the intensity fluctuation brought by turbulence in a system for compressed-sensing computational ghost imaging (CSCGI).

A variety of intensity-fluctuation turbulence channel models, e.g. log-normal, negative exponential, and gamma-

*Corresponding author: lh Zhang@usst.edu.cn, ORCID 0000-0002-1787-2978

Color versions of one or more of the figures in this paper are available online.



This is an Open Access article distributed under the terms of the Creative Commons Attribution Non-Commercial License (<http://creativecommons.org/licenses/by-nc/4.0/>) which permits unrestricted non-commercial use, distribution, and reproduction in any medium, provided the original work is properly cited.

gamma, were proposed to analyze the effects of turbulence on a free-space optical (FSO) communication system [13-16]. Among the above models, the gamma-gamma intensity-fluctuation model has been most widely applied in analyzing the BER of a communication (transmission) system, since it can fit a broad range of turbulence conditions (from weak to strong) [17]. In CGI, the key to receiving the transmitted images is to obtain a specific intensity value from a bucket detector. The value is the sum of intensity in the receiving area of the bucket detector. The PSNR and BER performance are directly related to the sum of intensity, as discussed above. Obviously, obtaining the received intensity in CGI is similar to that of an FSO system. Based on this common ground, it may be reasonable to apply the gamma-gamma intensity fluctuation model to analyze the PSNR and BER performance of the CGI system.

The rest of this paper is organized into three sections: The theories of CSCGI and atmospheric turbulence channel are expressed in Sections 2.1 and 2.2 respectively. Then, the scheme for the CSCGI system under GG atmospheric turbulence channel is discussed in Section 2.3. Accordingly, in Section III, PSNR and BER are simulated to measure the performance of the proposed scheme. The PSNR and BER performance are determined by the refractive-index structure parameter C_n^2 , the transmission distance d , and the sampling rate N , as further discussed in Sections 3.1 to 3.3. At last, the conclusion of the whole work is presented in Section VI.

II. THEORETICAL ANALYSIS AND SCHEME DESCRIPTION

2.1. Theory of Compressed-sensing Computational Ghost Imaging

Ghost imaging, also known as correlated imaging or two-photon imaging, is a quantum or classical correlation feature based on light-field fluctuations. By measuring the intensity correlation function between the reference light field and the target-detection light field, a novel imaging technique that acquires target image information nonlocally is achieved. Correlated imaging is different from general, classical optical imaging, and can be independent of the speed of light; this is an important feature that distinguishes quantum optics from classical theory. It is a new type of imaging technology, but image resolution and contrast are still the most important technical objectives.

Traditional correlation imaging requires two optical paths, causing problems such as experimental difficulties and occupying a large space. To solve these problems, Shapiro proposed computational ghost imaging (CGI) [18], and Bromberg *et al.* improved CGI. Instead of rotating the ground glass, we applied a spatial light modulator to simplify the two light paths into one [19]. The principle of computational ghost imaging is shown in Fig. 1. The most

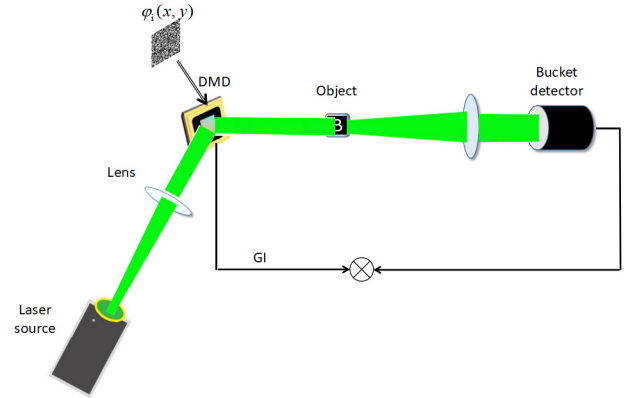


FIG. 1. Schematic diagram of computational ghost imaging.

important device in computational ghost imaging is the digital micromirror device (DMD), which is placed on the optical path where the object is located and controlled to produce a series of photos with random intensity or random phase. A bucket detector with no spatial resolution is used to receive the total intensity of the light field after the light has passed through the object [20].

While the computational ghost imaging is running, a series of random modulation matrices $\phi_i(x, y)$ are loaded onto the DMD. When the laser is irradiated on the DMD, the modulated light is reflected onto the object $D(x, y)$. Then the object is imaged, and the light transmitted through it is detected by the bucket detector (only when the light has passed through the object will the total intensity, without any resolution, be detected), and the total intensity I_i is calculated as shown in Eq. (1). Here the index i indicates sample number. After sampling z times, the modulation matrix and the value from the bucket detector are correlated, and the image of the object can be recovered. The correlation function $C_{CGI}(x, y)$ is expressed in Eq. (2).

$$I_i = \int \phi_i(x, y) \times D(x, y) dx dy, \quad (1)$$

$$C_{CGI}(x, y) = \frac{1}{z} \sum_{i=1}^z (I_i - \langle I \rangle) \phi_i(x, y). \quad (2)$$

Here $\langle I \rangle$ is the average value of light intensity, and N is the number of samples.

To improve the quality of the reconstructed image, various algorithms are introduced on the basis of ghost imaging, and compressed sensing is one of them. Compressed sensing, also known as compressed sampling or sparse sampling, is a technique for finding sparse solutions for underdetermined linear systems. Compressed-sensing theory utilizes the sparse characteristics of the signal, and the amount of effective information required is much less than the sampling amount required by the Nyquist sampling theorem, which reduces

the amount of information collected, saves signal acquisition time, and still reconstructs high-precision images. Low sampling and high reconstruction have been achieved. Combining compressed sensing and ghost imaging, the number of samples has been effectively reduced and the quality of image reconstruction have been effectively improved [21].

The formula for compressed sensing is:

$$y = \varphi x, \quad (3)$$

x is the original one-dimensional signal of length N . φ is the observation matrix, used to project the original high-dimensional signal x into the low-dimensional space; y is the one-dimensional measurement of length M . The measured value y and the measurement matrix φ are known, and the original signal x is obtained by solving the equation. In our scheme, x is a sparse signal.

In computational ghost imaging, the intensity I_i is recorded by the bucket detector as expressed in Eq. (4). Here “/” refers to the symbol of divisibility, and I_i is equal to the measured value y in Eq. (3), while the random matrix $\phi_i(x, y)$ used in each measurement is stretched into a row vector as the observation matrix φ of Eq. (3), and the intensity of the object $D(x, y)$ for imaging is equal to the intensity of the original signal x in Eq. (3).

$$\begin{bmatrix} I_1 \\ I_2 \\ \vdots \\ I_i \\ \vdots \\ I_{L_{z \times 1}} \end{bmatrix} = \begin{bmatrix} \phi_1(1,1) \dots \phi_1(1,y) \dots \phi_1(2,1) \dots \phi_1(x,y) \\ \phi_2(1,1) \dots \phi_2(1,y) \dots \phi_2(2,1) \dots \phi_2(x,y) \\ \vdots \\ \phi_i(1,1) \dots \phi_i(1,y) \dots \phi_i(2,1) \dots \phi_i(x,y) \\ \vdots \\ \phi_{L_{z \times 1}}(1,1) \dots \phi_{L_{z \times 1}}(1,y) \dots \phi_{L_{z \times 1}}(2,1) \dots \phi_{L_{z \times 1}}(x,y) \end{bmatrix} \begin{bmatrix} D(1,1) \\ D(1,2) \\ \vdots \\ D(1+i/\sqrt{z}, i \bmod \sqrt{z}) \\ \vdots \\ D(x,y) \end{bmatrix} \quad (4)$$

2.2. Theory of Atmospheric Turbulence Channel Model

The upper atmosphere's pressure and temperature are affected by wind and other factors. Accordingly, the refractive index of an optical path varies, and atmospheric turbulence occurs. This turbulence results in intensity fluctuations of the received signal, and increases the BER.

There are two methods to simulate turbulence: The first method is to study the effect of atmospheric turbulence on light intensity, *i.e.* the distribution model of light intensity. The second method is to generate Kolmogorov phase screens, which are based on the Kolmogorov spectrum.

In ghost imaging, there is a bucket detector receiving the total intensity of the transmission image, while the resolution and phase of each pixel in the image is not mainly a concern. As a result, we apply the first method, namely the distribution model, to simulate turbulence. The log-normal and gamma-gamma models are classical models to describe light-intensity distribution. The former is valid for weak turbulence, while the gamma-gamma distribution could be a better choice for a broad range of turbulences

(from weak to strong), because both large-scale and small-scale intensity fluctuations can be approximated by gamma distributions.

The gamma-gamma distribution is as follows [17]:

$$p(I) = \frac{2(\alpha\beta)^{(\alpha+\beta)/2}}{\Gamma(\alpha)\Gamma(\beta)} I^{(\alpha+\beta)/2-1} K_{\alpha-\beta} [2(\alpha\beta I)^{1/2}], \quad I > 0, \quad (5)$$

$$\alpha = \frac{1}{\sigma_x^2} \cong \left\{ \exp \left[\frac{0.49\sigma_1^2}{(1+1.11\sigma_1^{12/5})^{7/6}} \right] - 1 \right\}^{-1}, \quad (6)$$

$$\beta = \frac{1}{\sigma_y^2} \cong \left\{ \exp \left[\frac{0.51\sigma_1^2}{(1+0.69\sigma_1^{12/5})^{7/6}} \right] - 1 \right\}^{-1}.$$

In Eq. (6), $\sigma_1^2 = 1.23C_n^2 k^{7/6} L^{11/6}$ and C_n^2 is the refractive-index structure parameter. The degree of atmospheric refractive-index fluctuation is measured by C_n^2 , which varies with altitude and wind speed. In the ITU (International Telecommunication Union) -R H-V model, the relationship between $C_n^2(h)$ and altitude h is expressed in Eq. (7) and Fig. 2 [22, 23]. The conditions are set as $v_{RMS} = \{11, 21, 31\}$ and $C_n^2(0) = \{10^{-13}, 10^{-15}, 10^{-17}\}$:

$$C_n^2(h) = 8.148 \times 10^{-56} v_{RMS}^2 h^{10} e^{-h/1000} + 2.7 \times 10^{-16} e^{-h/1500} + C_{n0}^2 e^{-h/100}. \quad (7)$$

It can be seen from Fig. 2 that C_n^2 is approximately invariant with h when h is larger than 1000 m, and also considered approximately invariant with v_{RMS} when h is lower than 4000 m.

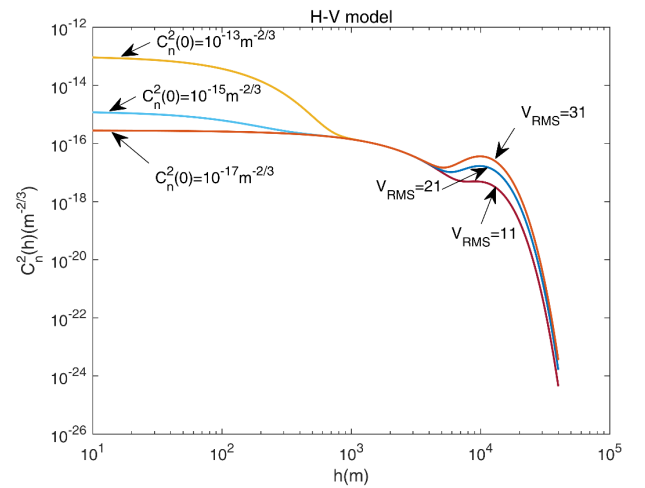


FIG. 2. The relationship of C_n^2 and h according to the H-V model.

In this paper, transmission in the horizontal path is researched, so C_n^2 is practically constant. The values of C_n^2 for the different turbulence regimes are as follows:

$$\begin{aligned} C_n^2 &= 10^{-17} m^{-2/3} \text{ for weak turbulence} \\ &= 10^{-15} m^{-2/3} \text{ for moderate turbulence} \\ &= 10^{-13} m^{-2/3} \text{ for strong turbulence.} \end{aligned}$$

2.3. Scheme of the Compressed-sensing Computational Ghost-imaging Transmission System Based on the Gamma-gamma Turbulence Channel

A schematic diagram of image transmission in compressed-sensing computational ghost imaging with the added turbulence model is shown in Fig. 3. After being modulated by the modulation matrix ϕ_i of the DMD, the laser passes through the object $O(x, y)$, then passes through the turbulent air mass $\varphi_i(x, y)$, and is finally received by the bucket detector. After the correlation calculation, the original image is reconstructed. The compressed-sensing computational ghost-imaging transmission based on the gamma-gamma turbulence channel model (GG-CSCGI) is expressed in Fig. 3.

The received light intensity is obtained from Eq. (8), considering the gamma-gamma turbulence in Eq. (5):

$$I_i = \int \phi_i(x, y) \times O(x, y) \times \varphi_i(x, y) dx dy. \quad (8)$$

Here $\phi_i(x, y)$ is the i^{th} modulation matrix, $O(x, y)$ is a function used to describe the light intensity of the object, and $\varphi_i(x, y)$ is multiplicative noise with a gamma-gamma distribution.

Next we bring the turbulence receiving function of the bucket detector into the compressed-sensing computational ghost imaging of Eqs. (4) and (8) to get the intensity array of the reconstructed image, as shown in Eq. (9):

$$\begin{bmatrix} O(1,1) \\ O(1,2) \\ \vdots \\ O(1+i/\sqrt{z}, i \bmod \sqrt{z}) \\ \vdots \\ O(x, y) \end{bmatrix}_{z \times 1} = \begin{bmatrix} \phi_1(1,1) \dots \phi_1(1,y) \dots \phi_1(2,1) \dots \phi_1(x,y) \\ \phi_2(1,1) \dots \phi_2(1,y) \dots \phi_2(2,1) \dots \phi_2(x,y) \\ \vdots \\ \phi_i(1,1) \dots \phi_i(1,y) \dots \phi_i(2,1) \dots \phi_i(x,y) \\ \vdots \\ \phi_z(1,1) \dots \phi_z(1,y) \dots \phi_z(2,1) \dots \phi_z(x,y) \end{bmatrix}_{z \times z}^{-1} \begin{bmatrix} I_1 \\ I_2 \\ \vdots \\ I_i \\ \vdots \\ I_z \end{bmatrix}_{z \times 1} \quad (9)$$

Here z is the total number of samples, $\phi_i(x, y)$ is a row vector that is stretched by the modulation matrix for each sample, and I_i the values received by the bucket detector, which can be calculated using Eq. (8). Researching how to set appropriate parameters in the GG-CSCGI system is the key to eliminating the negative influence of atmospheric turbulence and improving imaging quality. The PSNR and BER performance are discussed in the following section.

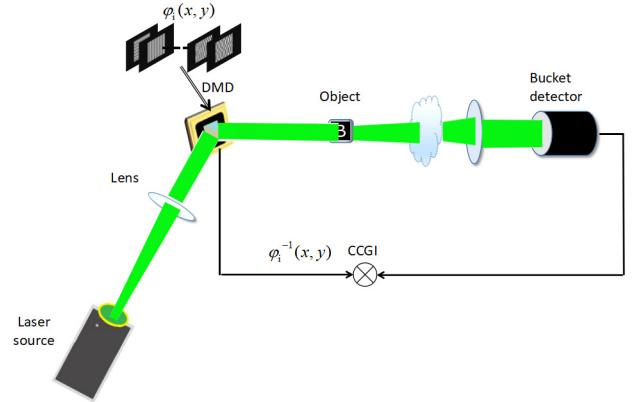


FIG. 3. Schematic diagram of the GG-CSCGI system.

III. SIMULATION OF THE COMPRESSED-SENSING COMPUTATIONAL GHOST-IMAGING TRANSMISSION SYSTEM BASED ON THE GAMMA-GAMMA TURBULENCE CHANNEL

In the simulation, a 64×64 -pixel binary image (letters “USST”, white on black) for correlation imaging has been selected, and the multiplicative gamma-gamma model of turbulence has been introduced. Three parameters—the transmission distance d , refractive-index structure parameter C_n^2 , and sampling rate N (which is defined as the ratio of sampling times to the total number of pixels)—are varied, to study the effect of atmospheric turbulence on correlated CSCGI.

In the simulation, we use the *gamrnd* function in Matlab to generate the gamma-gamma RV matrix, according to Eq. (5). The parameters α and β are calculated by Eq. (6), and the RV matrix is used as the multiplicative factor added into the correlation imaging system.

To detect the quality of the reconstructed image, two objective evaluation indicators, PSNR and BER, are used. Since the original image is a 64×64 binary image with only 4096 points, the image should be repeated to simulate enough points and calculate a sufficiently low BER. PSNR is an objective evaluation indicator for image quality, most commonly used in image processing. After compression, transmission, and other operations, the processed image usually differs from the original image. To measure the quality of the processed image, the PSNR value is usually used to determine whether the compressed transmission process conforms to the standard. PSNR is typically used for comparison of the maximum of the signal to the background noise. The larger the PSNR value between the two images, the less the distortion, and the more similar the two images are. PSNR can be calculated by Eqs. (10) and (11) as follows:

$$MSE = \frac{1}{mn} \sum_{i=0}^{m-1} \sum_{j=0}^{n-1} \|D(i, j) - Rd(i, j)\|^2, \quad (10)$$

$$PSNR = 10 \cdot \log_{10} \left(\frac{MAX_I^2}{MSE} \right) = 20 \cdot \log_{10} \left(\frac{MAX_I}{\sqrt{MSE}} \right). \quad (11)$$

Here MSE is the mean square error between the original image and the output image, and MAX_I indicates the maximum value of the image color. In this experiment binary images are transmitted, so the value of MAX_I is taken to be 1.

BER is also an indicator of the accuracy and reliability of a transmission system. It is defined as the ratio of the number of error bits to the number of all transmitted bits, as expressed in Eq. (12):

$$P_e = \frac{\text{number of the error bits}}{\text{number of all transmission bits}} * 100\%. \quad (12)$$

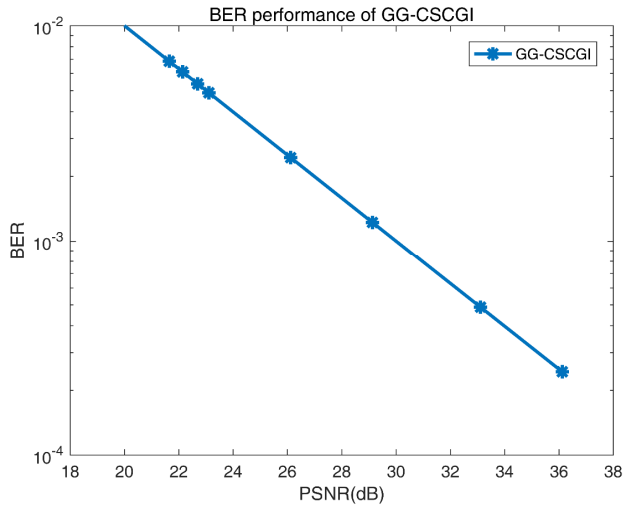


FIG. 4. BER performance of GG-CSCGI.

In this article, Eq. (12) is specified as:

$$P_e = \frac{N_{Y_{xy}-X_{xy}}}{x \times y}. \quad (13)$$

$N_{Y_{xy}-X_{xy}}$ is the number of input and output pixels with nonzero difference, and $x \times y$ is the total number of pixels.

In Fig. 4, the relationship between the PSNR and the BER of a GG-CSCGI system is expressed. To eliminate the inherent error of the associated imaging, N is set as the full sampling rate, namely 100%. Let the peak power of the transmitted binary signal be 1, and the noise power be the variance of the multiplicative turbulence noise; thus the PSNR can be obtained. In addition, the value of PSNR can be varied by changing the key parameters of the turbulence channel, namely the refractive-index structure parameter C_n^2 and transmission distance d . This operation will be discussed in the following paragraphs. It can be seen from Fig. 4 that as PSNR increases, BER decreases. For PSNR values between 10 dB and 17 dB, the BER remains high ($>10^{-1}$). When the PSNR is greater than 17 dB, the BER obviously decreases. For each 1 dB increase in PSNR, the BER decreases by one order of magnitude, and it has dropped below 10^{-3} when the PSNR is 30 dB.

3.1. Analysis of the Influence under Different Conditions of Transmission Distance

To ensure that the associated imaging channel is only affected by turbulence, N is taken as 100%. When analyzing the influence under different transmission distances, the refractive-index structure parameter C_n^2 is taken as 10^{-13} , 10^{-15} , and 10^{-17} , and the distance between the transmitter and the receiver d is set to a series of values. Thus the according imaging effects at different d are shown in Table 1.

TABLE 1. Imaging effects for different transmission distances (in meters)

Distance d	400	350	300	250	200	150	100	Original
$C_n^2 = 10^{-13}$								
Distance d	4000	3500	3000	2500	2000	1500	1000	Original
$C_n^2 = 10^{-15}$								
Distance d	70000	60000	50000	40000	30000	20000	10000	Original
$C_n^2 = 10^{-17}$								

When $C_n^2 = 10^{-13}$ and the value of d ranges from 100 to 400 m, the imaging performance significantly changes from fine to bad. Similar significant changes in the imaging performance occur for the situations of $C_n^2 = 10^{-15}$ with d ranging from 1000 to 4000 m, and $C_n^2 = 10^{-17}$ with d ranging from 10,000 to 70,000 m. PSNR and BER performance with d are expressed in Fig. 5.

Obviously, as d increases PSNR rises, while BER declines. Both tend to stabilize when d increases to a specific value, which varies with C_n^2 .

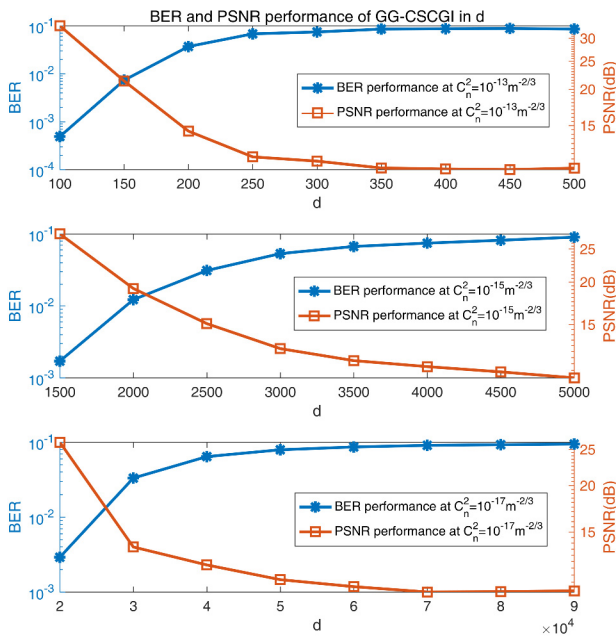


FIG. 5. BER and PSNR curves for various transmission distances.

3.2. Analysis of the Influence under Different Conditions of Refractive-index Structure Parameter

Similarly, when analyzing the influence of C_n^2 , N is also set to 100%. When analyzing the influence under different values of the refractive-index structure parameter, the transmission distance d is set to 100 m, 1000 m, and 10,000 m respectively, and C_n^2 is set to a series of values. Thus the according imaging effects for different d are shown in Table 2.

When $d = 100$ m and the range of C_n^2 is from 1×10^{-13} to 7×10^{-13} , the imaging performance significantly changes

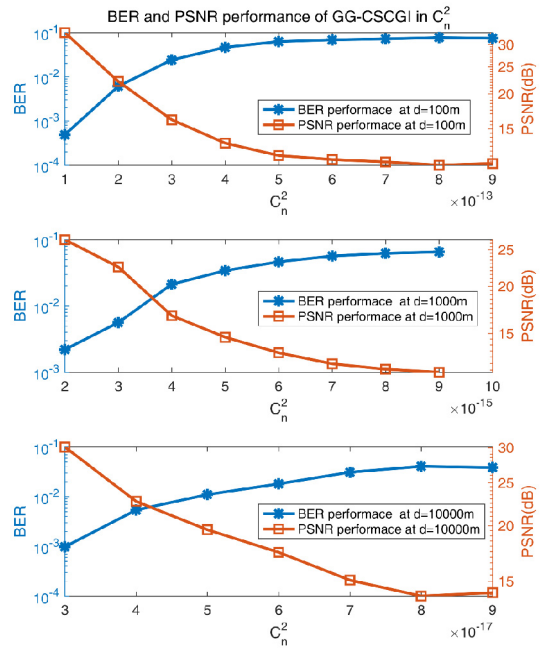


FIG. 6. BER and PSNR curves for different values of the refractive-index structure parameter C_n^2 .

TABLE 2. Imaging effects for different values of the refractive-index structure parameter C_n^2

C_n^2	7×10^{-13}	6×10^{-13}	5×10^{-13}	4×10^{-13}	3×10^{-13}	2×10^{-13}	1×10^{-13}	Original
$d = 100$								
C_n^2	7×10^{-15}	6×10^{-15}	5×10^{-15}	4×10^{-15}	3×10^{-15}	2×10^{-15}	1×10^{-15}	Original
$d = 1000$								
C_n^2	7×10^{-17}	6×10^{-17}	5×10^{-17}	4×10^{-17}	3×10^{-17}	2×10^{-17}	1×10^{-17}	Original
$d = 10000$								

from fine to bad. Similar significant changes in imaging performance occur in the situations with $d=1000$ m and C_n^2 ranging from 1×10^{-15} to 7×10^{-15} , and $d=10,000$ m and C_n^2 ranging from 1×10^{-17} to 7×10^{-17} . PSNR and BER performance with varying C_n^2 are expressed in Fig. 6.

The trend in Fig. 6 is opposite than that in Fig. 5: As C_n^2 increases, PSNR rises, while BER declines. Both tend to stabilize when C_n^2 increases to a specific value that varies with d .

3.3. Analysis of the Influence under Different Conditions of Sampling Rates

Next the refractive-index structure parameter C_n^2 is taken as 1×10^{-15} and the distance d as 2000 m, and the sampling rate N of the associated imaging is adjusted, to observe the influence of turbulence for different N .

The corresponding image effects are shown in Table 3, and the PSNR and BER performance with varying N are expressed in Fig. 7.

When N is very low, whether turbulence is considered or not, the imaging is not satisfactory. When $N=15\%$, the reconstructed image is noisy, almost regardless of whether













turbulence is added or not. When $N=35\%$, both cases return an identifiable original image, but there is much noise; the reconstructed image without turbulence is better than the reconstructed image with turbulence. When $N=100\%$, the compressed sensing has completely restored the original image without noise, and the images for turbulent compressed sensing also present the clear letters of the original image, though a small amount of noise is still visible. In the simulation, the compressed sensing significant suppresses the negative effect of turbulence, and when N is sufficient, the image can be restored very well.

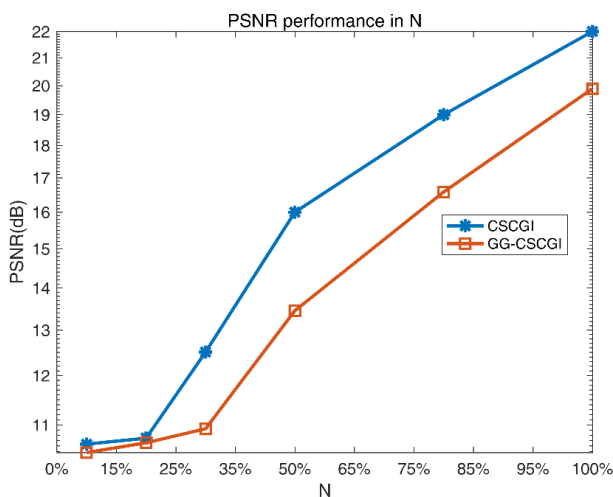
As N increases, PSNR rises, while BER declines. In addition, the PSNR of the reconstructed image without turbulence is higher than that of the reconstructed image considering turbulence, while the corresponding BER without turbulence is much lower than that considering turbulence.

IV. CONCLUSION

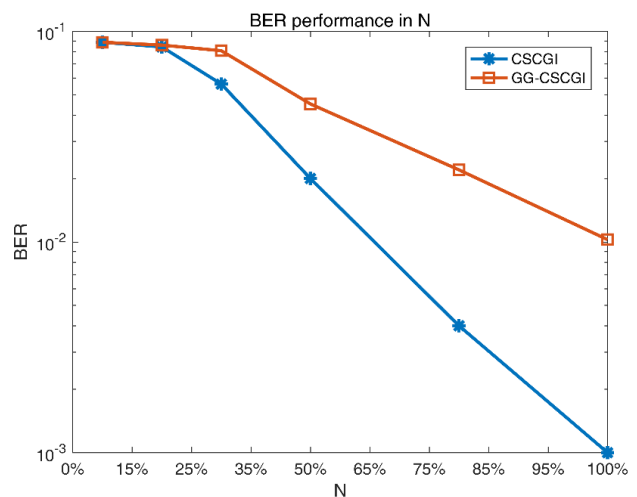
In this paper, the BER performance of a compressed-sensing computational ghost-imaging system based on the gamma-gamma atmospheric turbulence channel model has

TABLE 3. Imaging effects under different sampling rates

Sampling rate N	15%	25%	35%	50%	75%	100%
CSCGI						
GG-CSCGI						



(a)



(b)

FIG. 7. (a) PSNR curves and (b) BER curves for different sampling rates N .

been researched. The influence of light intensity for the gamma-gamma atmospheric turbulence channel on image transmission has been analyzed. Specifically, the intensity influence is mediated by the key parameters of the turbulence channel, namely the refractive-index structure parameter C_n^2 and transmission distance d . Simulation results have shown that the key parameters are both negatively correlated with PSNR and positively correlated with BER. The PSNR and BER approach certain constants and then are stable when either of the key parameters increases sufficiently. The whole work provides a theoretical model basis and reference for a practical ghost-imaging system transmitting through an atmospheric turbulence channel.

ACKNOWLEDGMENT

This research was funded by the National Nature Science Foundation of China (No. 61805144), Shanghai Sailing Program (No. 17YF1429400), Natural Science Foundation of Shanghai (Grant Nos. 18ZR1425800 and 14ZR1428400), and the National Natural Science Foundation of China (Grant Nos. 61875125 and 61405115).

REFERENCES

1. T. B. Pittman, Y. H. Shih, D. V. Strekalov, and A. V. Sergienko, "Optical imaging by means of two-photon quantum entanglement," *Phys. Rev. A* **52**, R3429(R) (1995).
2. R. E. Meyers and K. S. Deacon, "Quantum ghost imaging experiments at ARL," *Proc. SPIE* **7815**, 78150I.
3. J. H. Shapiro, "Computational ghost imaging," *Phys. Rev. A* **78**, 061802(R) (2008).
4. X. Bai, Y. Q. Li and S. M. Zhao, "Differential compressive correlated imaging," *Acta Phys. Sin.* **62**, 44209-044209 (2013).
5. F. Ferri, D. Magatti, L. A. Lugiato, and A. Gatti, "Differential ghost imaging," *Phys. Rev. Lett.* **104**, 253603 (2010).
6. P. Zhang, W. Gong, X. Shen, and S. Han, "Correlated imaging through atmospheric turbulence," *Phys. Rev. A* **82**, 33817 (2010).
7. R. E. Meyers, K. S. Deacon and Y. Shih, "Turbulence-free ghost imaging," *Appl. Phys. Lett.* **98**, 111115 (2011).
8. L. Zhang, Y. Hualong, and D. Zhang, "Study on the key technology of image transmission mechanism based on channel coding ghost imaging," *IEEE Photonics J.* **10**, 6500913 (2018).
9. L. Zhang, Y. Hualong, D. Zhang and J. Chen, "Study on image transmission mechanism of ghost imaging based on joint source and channel coding," *Appl. Phys. B* **125**, 57 (2019).
10. X. Liu, F. Wang, M. Zhang, and Y. Cai, "Effects of atmospheric turbulence on lensless ghost imaging with partially coherent light," *Appl. Sci.* **8**, 1479 (2018).
11. J. Cheng, "Ghost imaging through turbulent atmosphere," *Opt. Express* **17**, 7916-7921 (2009).
12. N. D. Hardy and J. H. Shapiro, "Reflective ghost imaging through turbulence," *Phys. Rev. A* **84**, 063824 (2011).
13. J. Parikh and V. K. Jain, "Study on statistical models of atmospheric channel for FSO communication link," in *Proc. Nirma University International Conference on Engineering* (Ahmedabad, India, Dec. 2011). pp. 1-7.
14. S. Arnon, "Effects of atmospheric turbulence and building sway on optical wireless-communication systems," *Opt. Lett.* **28**, 129-131 (2003).
15. J. Dai, X. G. Bai and H. Shu, "Coordination of multi-leaders and multi-followers in supply chain of value-added telecom services," *Chin. Commun.* **8**, 157-164 (2011).
16. W. O. Popoola, Z. Ghassemlooy and V. Ahmadi, "Performance of sub-carrier modulated free-space optical communication link in negative exponential atmospheric turbulence environment," *Int. J. Auton. Adapt. Commun. Syst.* **1**, 342-355 (2008).
17. A. Al-Habash, L. C. Andrews, and R. L. Phillips, "Mathematical model for the irradiance probability density function of a laser beam propagating through turbulent media," *Opt. Eng.* **40**, 1554-1563 (2001).
18. B. I. Erkmén and J. H. Shapiro, "Unified theory of ghost imaging with gaussian-state light," *Phys. Rev. A* **77**, 043809 (2008).
19. Y. Bromberg, O. Katz and Y. Silberberg, "Ghost imaging with a single detector," *Phys. Rev. A* **79**, 053840 (2009).
20. T.-Y. Mao, Q. Chen, W.-J. He, J.-Y. Zhuang, Y.-H. Zou, H.-D. Dai, and G.-H. Gu, "Optical communication in turbid and turbulent atmosphere," *Acta Phys. Sin.* **65**, 084207 (2016).
21. Z. Liu, S. Tan, J. Wu, E. Li, X. Shen and S. Han, "Spectral camera based on ghost imaging via sparsity constraints," *Sci. Rep.* **6**, 25718 (2016).
22. Z. Ghassemlooy, W. Popoola, and S. Rajbhandari, *Optical Wireless Communications System and Channel Modelling with MATLAB* (CRC Press, New York, USA, 2012).
23. ITU-R, *P.618: Propagation data and prediction methods required for the design of Earth-space telecommunication systems* (International Telecommunication Union, 2017), <https://www.itu.int/rec/R-REC-P.618-13-201712-I/en>.